Nonvolatile Tuning of Bragg Structures Using Transparent Phase-Change Materials

NICHOLAS A. NOBILE,[1,†] CHUANYU LIAN,[2,3,†] HONGYI SUN,[2,3] YI-SIOU HUANG,[2,3] BRIAN MILLS,[4,5] COSMIN CONSTANTIN POPESCU,[4] DENNIS CALLAHAN,[6] JUEJUN HU,[4] CARLOS A. RÍOS OCAMPO,[2,3] AND NATHAN YOUNGBLOOD[1,*]

[1]Electrical & Computer Engineering Department, The University of Pittsburgh, Pittsburgh, PA 15213, USA
[2]Department of Materials Science & Engineering, University of Maryland, College Park, MD 20742, USA
[3]Institute for Research in Electronics & Applied Physics, University of Maryland, College Park, MD 20742, USA
[4]Department for Materials Science & Engineering, Massachusetts Institute of Technology, Cambridge, MA 02139, USA
[5]Draper Scholar Program, The Charles Stark Draper Laboratory, Inc, Cambridge, MA, 02139
[6]The Charles Stark Draper Laboratory, Inc, Cambridge, MA, 02139
[†]These authors contributed equally
*nathan.youngblood@pitt.edu

Abstract: Bragg gratings offer high-performance filtering and routing of light on-chip through a periodic modulation of a waveguide's effective refractive index. Here, we model and experimentally demonstrate the use of Sb_2Se_3, a nonvolatile and transparent phase-change material, to tune the resonance conditions in two devices which leverage periodic Bragg gratings—a stopband filter and Fabry-Perot cavity. Through simulations, we show that similar refractive indices between silicon and amorphous Sb_2Se_3 can be used to induce broadband transparency, while the crystalline state can enhance the index contrast in these Bragg devices. Our experimental results show the promise and limitations of this design approach and highlight specific fabrication challenges which need to be addressed in future implementations.

1. Introduction

Wavelength division multiplexing (WDM) with frequency selective routing, filtering, and modulation is one of the core advantages of optics over electronics for data transmission. Today, modern optical filtering can demand the control of over >100 channels within a small range of wavelengths from about 1525 nm to 1610 nm according to current DWDM standards. This level of spectral control for optical routing has grown to become the backbone of data sent locally within data centers and globally in transatlantic fiber communications. Spectrally selective control of light on-chip is equally important for a variety of commercial and emerging applications, such as on-chip laser cavities [1], [2], resonant modulators [3], pulse shaping [4], LiDAR [5], [6], and even computing [7]–[10]. One simple, yet powerful technique to control the wavelength-dependent response of an optical signal is through Bragg gratings which are typically fabricated using periodic perturbations to the waveguide width [11]. By changing the period and modulating the strength of these perturbations, the bandwidth and central frequency of the Bragg grating can be controlled [12]. Additionally, filters comprised of Bragg gratings are not limited in channel density by free spectral range (FSR) effects which are an issue for microring-based WDM filter banks [13].

Due to the fixed nature of geometric patterning, the tunability of Bragg gratings is limited after fabrication. Thermo-optic or electro-optic effects can be used to tune the resonance condition within a limited range [3], [14], [15], although they are volatile and require constant power supply to tune the device. Creating reconfigurable, nonvolatile photonic filters could simplify system design and enable multi-functionality within the same circuit on-chip.

Additionally, the grating profile on-chip can be subject to fabrication variations and nonvolatile methods for tuning the resonance frequency of these Bragg gratings could be important for aligning multiple Fabry-Perot (FP) resonators or contra-directional couplers on-chip [3], [8]. Low-loss phase-change materials, such as Sb_2Se_3 and Sb_2S_3, are ideal for this application as the high index contrast between the amorphous and crystalline phases can be used to create a periodic index perturbation or tune the resonance of a Bragg grating [16]–[18]. Switching between the amorphous and crystalline states can be achieved thermally, where thermal excitation from an electrical or optical pulse heats the material above its melting or crystallization temperature to induce a nonvolatile phase transition. While compared to faster phase-change materials (PCMs) such as $Ge_2Sb_2Te_5$ [19], Sb_2Se_3 exhibits a slower crystallization speed (several microseconds or longer [20], [21]) and reversible switching beyond a few thousands of cycles has yet to be demonstrated. However, the exceptionally low optical loss of Sb_2Se_3 in both amorphous and crystalline states allows phase-only tuning of nanophotonic devices with minimal added absorption [20]–[24]. For example, prior experimental results using $Ge_2Sb_2Te_5$ to tune the filter response of Bragg gratings show that the high absorption in the crystalline state limits the spectral performance of these devices and increases insertion loss [25], [26].

Phase-Change Material	Change in RI (Δn @ 1550 nm)	Max. Absorption Coefficient (k)	Crystallization Speed	Cycling Endurance
$Ge_2Sb_2Te_5$	3.34	1.88	< 50 ns [27]	>10^6 [28]
$Ge_2Sb_2Se_4Te_1$	1.76	0.35	1 – 10 ms [29]	>10^4 [29]
$Ge_2Sb_2Se_5$	0.43	0.14	>100 ms [30]	>10^5 [30]
Sb_2Se_3	0.76	0.0035	0.1 – 1 ms [21]	>10^3 [24]
Sb_2S_3	0.59	0.0026	0.1 – 1 ms [31]	>10^3 [31]

Table 1: Comparison of five well known optical phase-change materials. For tuning Bragg gratings, it is desirable to have a high change in refractive index (RI) with low maximum absorption coefficient (k). Values for both Δn and k are reported for a wavelength of 1550 nm from references [21], [22], [32].

Here, we propose and experimentally explore the ability to switch from an enabled to a disabled Bragg resonance within a periodic device that is functionalized with the phase-change material Sb_2Se_3. Through eigenmode simulations and transfer matrix method (TMM) modeling of these devices, we show that it is possible to use the large and transparent index contrast of Sb_2Se_3 to either amplify or cancel out the effective index contrast of a Bragg grating by carefully designing the width of the waveguide with and without Sb_2Se_3. Additionally, we show that the large index contrast between the amorphous and crystalline states can be used to tune the FP resonance of a phase-shifted Bragg grating and even completely move it beyond the stopband of the grating under certain design conditions.

2. Designing tunable Bragg gratings with phase-change materials

Fig. 1a illustrates the overall concept of our design approach. A Bragg grating with Sb_2Se_3 embedded in the waveguide (dark blue and red regions) can either cancel or enhance the periodic perturbation of the effective refractive index of the waveguide. When the effective refractive index of waveguide with amorphous Sb_2Se_3 matches that of the silicon waveguide without Sb_2Se_3, the effective index perturbation is canceled, and the device appears to the propagating optical mode as if no grating exists. However, after crystallization, the regions with embedded Sb_2Se_3 further enhance the index contrast and perturbation from the patterned Bragg grating is increased. This effect is directly related to fact that in the amorphous state, Sb_2Se_3 has a slightly lower refractive index than silicon ($n_{am} = 3.27$ at $\lambda = 1550$ nm) while in the crystalline state the refractive index is higher than that of silicon ($n_{cry} = 4.04$ at $\lambda = 1550$ nm). The refractive indices of Sb_2Se_3 thin films before and after crystallization were measured using ellipsometry and are shown in Fig. 1b.
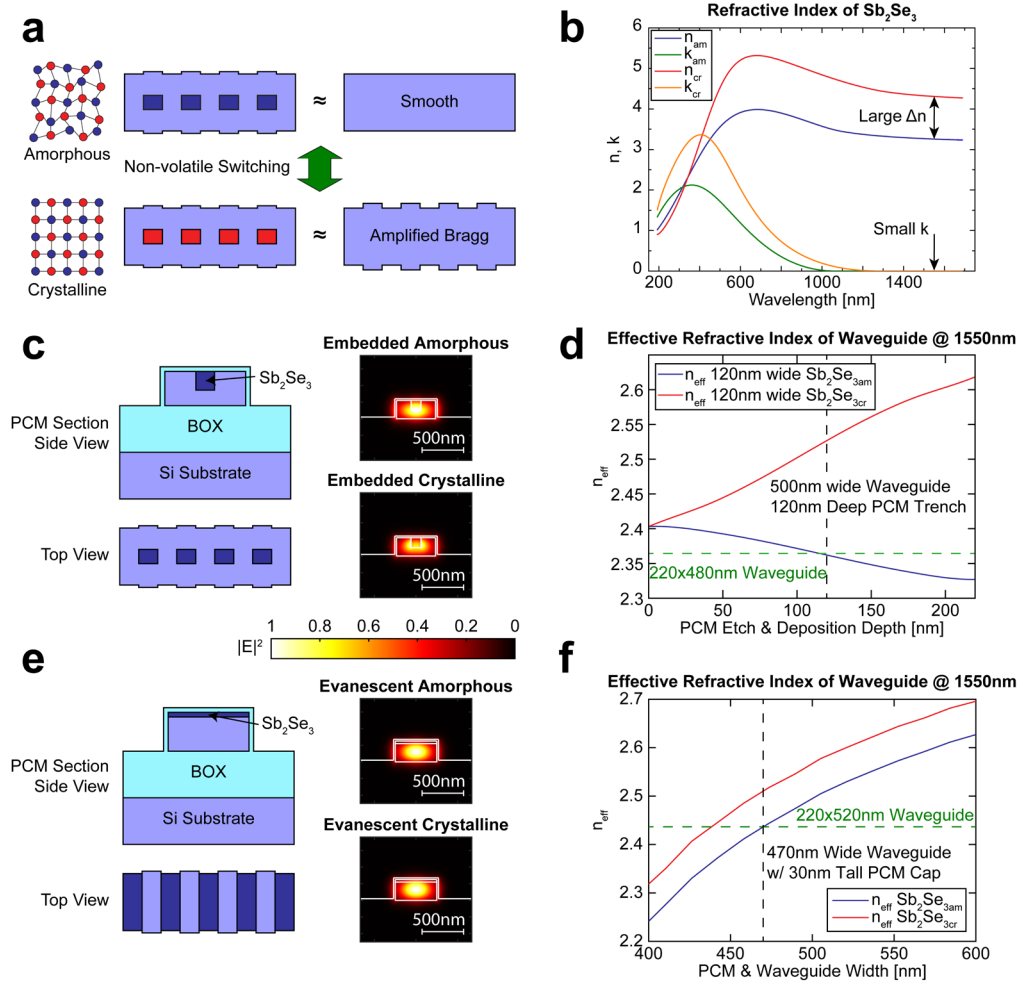
Fig. 1. (a) Proposed concept for switching between a resonant Bragg grating with enhanced index contrast (bottom) and broadband transmission with no periodic index contrast (top) using the nonvolatile phase transition of Sb$_2$Se$_3$. (b) Measured refractive index for as-deposited (amorphous) Sb$_2$Se$_3$ and annealed (crystalline) Sb$_2$Se$_3$ using thin-film ellipsometry. (c-d) Illustration of Sb$_2$Se$_3$ embedded in the waveguide or (e-f) deposited on top of the waveguide. The effective refractive index of the combined waveguide-Sb$_2$Se$_3$ system in both the crystalline and amorphous states is shown in the graphs (c) and (e) on the right. The design conditions where the effective refractive index of the waveguide with amorphous Sb$_2$Se$_3$ matches that of a waveguide without any Sb$_2$Se$_3$ is indicated by the intersection of the dashed green and black lines in the graphs (d) and (f) on the right.

We explored two design approaches to control the index perturbation of the Bragg gratings. The first design illustrated in Fig. 1c embeds the Sb$_2$Se$_3$ directly in the waveguide, replacing silicon in the embedded regions. Using Ansys Lumerical's eigenmode solver (MODE), we simulated the effective refractive index of a waveguide with Sb$_2$Se$_3$ of various widths embedded 120 nm into a standard 500 nm × 220 nm single mode silicon waveguide. For increasing Sb$_2$Se$_3$ widths, the effective refractive index decreases in the amorphous state (due to a lower refractive index compared to that of bulk silicon) and increases in the crystalline state. If we choose to replace a 120 nm × 120 nm section of the silicon waveguide with Sb$_2$Se$_3$, n_{eff} in the amorphous state is equivalent to that of a 480 nm × 220 nm silicon waveguide. Thus, patterning a Bragg grating in a 500-nm-wide silicon waveguide with a 20 nm wide sidewall perturbation and embedding amorphous Sb$_2$Se$_3$ in the 500-nm-wide sections results in a waveguide with no effective index perturbation and no Bragg resonance. Crystallization

changes n_{eff} significantly in the embedded regions with $\Delta n_{eff} \approx 0.165$ as shown in the righthand graph in Fig. 1d.

In addition to embedding the Sb$_2$Se$_3$ into the waveguide, we also considered a design with Sb$_2$Se$_3$ deposited directly on top of the waveguide as shown in Fig. 1e. This design is easier to fabricate but reduces the change in modulation strength of the Bragg grating to $\Delta n_{eff} \approx$ 0.074 since the interaction between the PCM and the optical mode is reduced to evanescent coupling. Additionally, since material is being added to the waveguide (rather than replacing the silicon), the effective refractive index is increased for both the amorphous and crystalline phases. Therefore, for this evanescently-coupled design, Sb$_2$Se$_3$ is added to the regions of the waveguide that are narrower than the plain silicon waveguide in order to maintain a constant n_{eff} in the amorphous phase. The conditions for effective index matching with a 520-nm-wide waveguide and the effective index change after crystallization are again shown in the righthand graph in Fig. 1f.

3.   Modeling Results

Modeling Bragg gratings with Sb$_2$Se$_3$

Using the n_{eff} results from Fig. 1c-d, we used the transfer matrix method (TMM) to simulate the spectra of our two proposed designs [11]. This modeling approach uses the Fresnel Equation which approximates the Bragg grating as a periodic step perturbation in the waveguide's n_{eff}. These simulations account for the dispersion of the waveguide geometry and refractive index of the Sb$_2$Se$_3$ in both states. Fig. 2a-b show the resulting spectra for the embedded design, while Fig. 2c-d are for the evanescently coupled design for $N = 100$, where N is the number of periods. While both designs can achieve broad transmission close to unity over the simulated 1.5–1.6 μm wavelength range, we see that the stopband in the crystalline state is significantly narrower with a lower peak reflection for the evanescently coupled design (Fig. 2c). This is due to the weaker modulation of Δn_{eff} compared to the embedded design which is directly related to the bandwidth of the Bragg grating [11]:

(1) $$\Delta\lambda = \frac{\lambda_B^2}{\pi n_g}\sqrt{\kappa^2 + (\pi/L)^2}, \text{ with } \lambda_B = 2\Lambda\bar{n}_{eff} \text{ and } \kappa = \frac{2\Delta n_{eff}}{\lambda_B},$$

where $\Delta\lambda$ is the bandwidth of the Bragg filter measured between the first nulls around resonance, λ_B is the central resonance wavelength, Λ is the grating period, $\bar{n}_{eff}$ is the average effective index of the grating, n_g is the group index, κ is the grating strength, Δn_{eff} is the difference in n_{eff} between the areas with and without Sb$_2$Se$_3$, and L is the length of the grating. For the case where the grating is sufficiently long relative to the grating strength (i.e., $\kappa \gg \pi/L$), the bandwidth simplifies to:

(2) $$\Delta\lambda \approx \lambda_B \left(\frac{2\Delta n_{eff}}{\pi n_g}\right)$$

From the above expression, we can see that $\Delta\lambda$ is directly proportional to Δn_{eff}. Thus, the reduction of $\Delta\lambda = 39.55$ nm in the embedded case (Fig. 2a) to $\Delta\lambda = 20.23$ nm in the evanescent case (Fig. 2c) is due to the ~2× decrease in Δn_{eff} which can be seen when comparing the n_{eff} plots in Fig. 1c-d. A weaker grating strength for a fixed grating length will also reduce the peak reflectivity at λ_B, which is equal to $R_{peak} = \tanh^2(\kappa L)$, as seen in the case of the evanescently coupled design. To account for this offset, the evanescent Bragg filter devices were fabricated instead with twice the number of periods as that of the embedded devices.
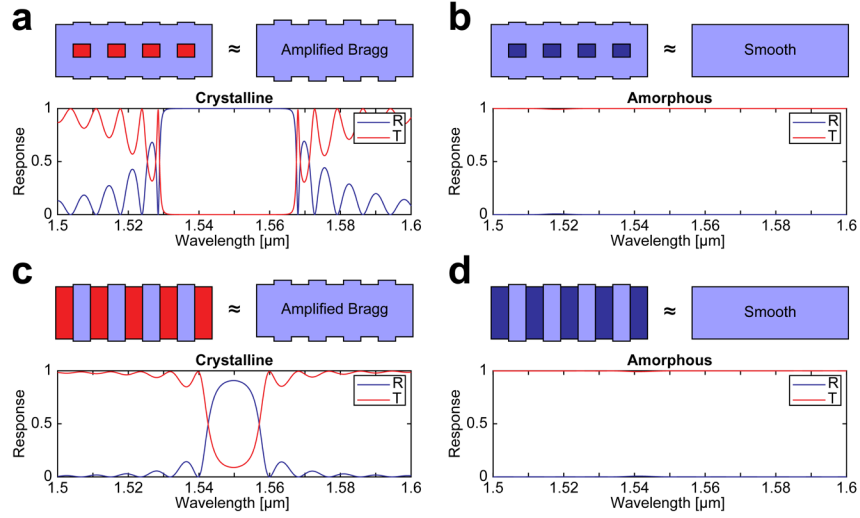
Fig. 2. (a)-(b) Simulated spectra of a Bragg grating with (a) crystalline and (b) amorphous Sb$_2$Se$_3$ embedded in the silicon waveguide grating. When the device is in the amorphous state as shown in (b), the transmission across the entire C-band and L-band is almost unity due to the precise matching of the effective refractive indices in the periodic structure. (c)-(d) Simulated spectra for the case of evanescently-coupled Sb$_2$Se$_3$ deposited on top of the waveguide for the (c) crystalline and (d) amorphous phases. All simulations used TMM to model the spectra and accounted for the wavelength dispersion of the refractive index for both silicon and Sb$_2$Se$_3$. The number of periods for all simulations was held constant at N = 100.

Modeling phase-shifted Bragg gratings with Sb$_2$Se$_3$

An FP cavity can be created by placing a phase-shift inducing defect with an optical path length equal to an odd number of half periods within a Bragg grating. The length of the defect without any PCM added can be written in terms of an integer number of odd periods:

$$(3) \qquad L_{defect} = \Lambda \left(m + \frac{1}{2} \right), \text{ where } m = 0, 1, 2, ...$$

where Λ is the period of the grating and m is a whole number. When a low-loss PCM is placed on the defect region, transitions between amorphous and crystalline phases will induce a resonance shift due to a change in n_{eff} as explored by other groups in previous works [16], [17]. In addition to tuning the resonance position, we can also fully shift the resonance out of the stopband of the cavity upon a phase transition, thus removing the defect entirely. For this effect to happen, the change in n_{eff} for the waveguide in the defect region must result in an odd multiple of π/2 phase shift for one of the phases while also providing an even multiple of π/2 phase shift in the other phase. Therefore, the length of the cavity can be designed at the first length to match the following condition:

$$(4) \qquad L_{defect} = \frac{m\lambda_B}{2n_{eff,p1}} = \frac{(m+\frac{1}{2})\lambda_B}{2n_{eff,p2}}, \text{ where } m = 0, 1, 2, ...$$

where $n_{eff,p1}$ is the n_{eff} of the FP defect waveguide in one of the PCM phases and $n_{eff,p2}$ the other. In order to center the resonance within the stopband, we can adjust the location of the stopband or the n_{eff} of the FP cavity waveguide. This means the grating period (Λ), average effective index of the grating ($\bar{n}_{eff}$), and the width of the FP cavity are the critical dimensions which must be chosen to satisfy the above condition. However, if the length of the defect is too long, multiple FP resonances will be present for both the amorphous and crystalline state since the free spectral range of the cavity will be smaller than the bandwidth of the stopband. This effect can be seen when comparing the evanescently-coupled FP design in Fig. 3c-d with that of the shorter embedded design in Fig. 3a-b. This constraint necessitates a low-loss PCM with

a large change in refractive index. We have previously demonstrated that only a ~11 μm length of Sb_2Se_3 can reversibly induce a π phase shift when deposited on silicon waveguides with integrated microheaters [21], making Sb_2Se_3 an ideal candidate for inducing transparency within the stopband of a phase-shifted Bragg grating.
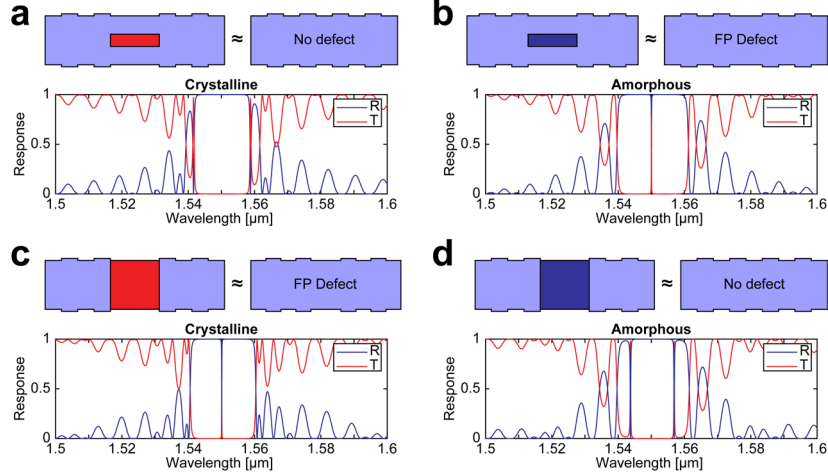

Fig. 3. (a)-(b) Simulated spectra of a phase-shifted Bragg grating with (a) crystalline and (b) amorphous Sb_2Se_3 embedded in the phase-shifted defect section. The length of the defect is chosen such that Δn_{eff} of the defect is equal to π when Sb_2Se_3 is switched between its amorphous and crystalline phases. (c)-(d) Spectra for a phase-shifted Bragg grating for an evanescently coupled design. The presence of a Fabry-Perot resonance in stopband when Sb_2Se_3 is in the crystalline phase is determined by whether the defect is equivalent to either an even or odd number of grating periods.

4.   Fabrication and Experimental Measurements

Devices were fabricated according to the designs shown in Fig. 2 and Fig. 3. The proposed designs were patterned using an ELS-G100 electron-beam lithography system on a silicon-on-insulator (SOI) platform (220 nm Si on 3 μm buried oxide from University Wafer) using ZEP positive resist. Reactive ion etching (RIE) in SF_6/C_4F_8 was then carried out to etch away 220 nm of Si. A 30 nm thin film of Sb_2Se_3 was thermally evaporated (120-nm-thick Sb_2Se_3 in the case of the embedded design) and a second electron-beam lithography step was used to pattern the Sb_2Se_3 layer using MaN-2403. The unexposed regions are subsequently etched away using RIE in CF_4 forming the Sb_2Se_3 patches on top of the waveguide and finally everything was capped using 10 nm of sputtered SiO_2 to avoid oxidation. A Santec TSL-570 tunable laser was used as the laser source and optical signals were collected by a Santec MPM-210 photodetector to capture transmission spectra of the Bragg devices. Amorphous measurements took place directly after fabrication. Devices were then crystallized using a hotplate at 250C for 10 minutes before being remeasured.
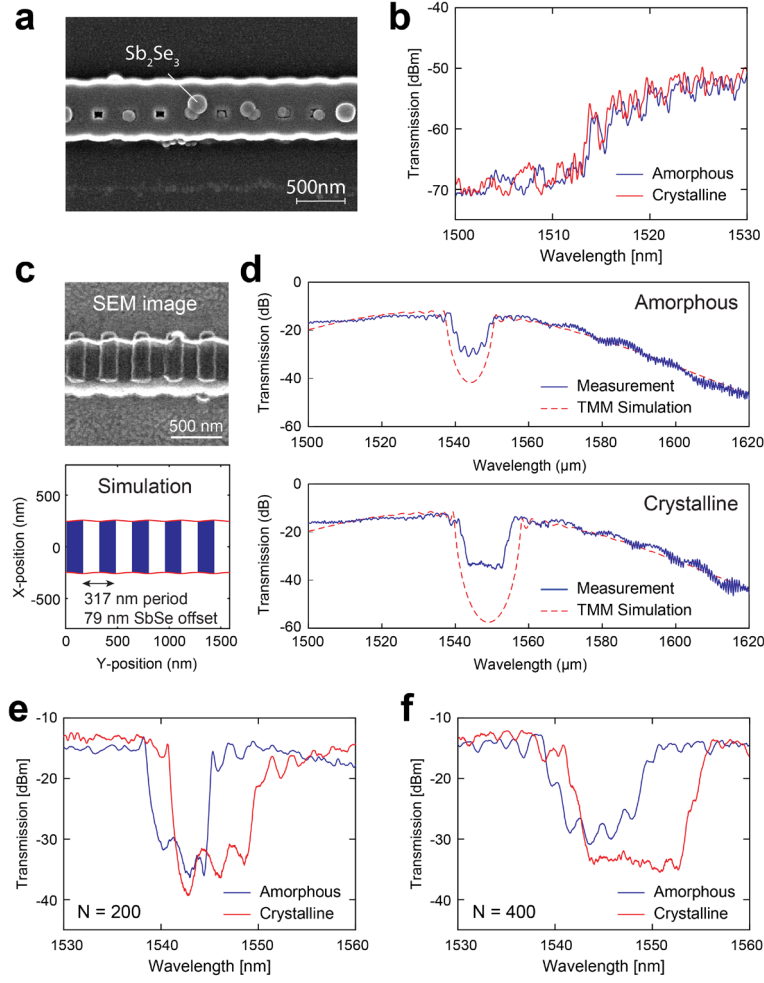
Fig. 4. Results of fabricated Bragg devices. (a) SEM image of fabricated device with Sb₂Se₃ designed to be embedded into the waveguide. The poor quality of the filling and nonuniformity of the Sb₂Se₃ in the waveguide resulted in minimal spectral shift after crystallization as shown in (b). (b) Measured spectra of device in (a) before and after annealing showing negligible phase shift and high scattering loss due to the unfilled waveguide holes. (c) Top: SEM image of fabricated device with Sb₂Se₃ evanescently coupled on waveguide segments of a Bragg grating. Bottom: Simulation geometry used to model nonideal alignment between the Sb₂Se₃ layer (blue) and Bragg grating (red outline). (d) Comparison of simulated versus measured spectra of device in (f) with Sb₂Se₃ deposited on top of the waveguide. The poor alignment between the Sb₂Se₃ and Bragg grating reduces effectiveness of the refractive index contrast after phase transition. (e-f) Example devices with (e) N = 200 and (f) N = 400 gratings exhibiting a red-shift in Bragg wavelength and increase in bandwidth upon crystallization.

Fig. 4a and 4c show SEM images of the fabricated devices. Both designs exhibit misalignment between the two electron-beam lithography steps (approximately ~80 nm offset in the x-direction and ~100 nm in the y-direction possibly due to mechanical stage drift) and lithographic smoothing, which affected all device types. The embedded PCM devices (see Fig. 4a) exhibit an incomplete and nonuniform filling of the trenches by the phase change material and passivation layer. As a result, the embedded PCM devices did not operate according to their design. We observed high insertion loss due to scattering, a significant blue shift in the Bragg wavelength due to the lower effective index of the unfilled waveguide holes, and negligible spectral shift after crystallization (see Fig. 4b). The evanescent PCM devices displayed unintentional alignment offsets between the Sb₂Se₃ and photonic device layers (Fig.

4c) which reduced functionality. The lower inset of Fig. 4c shows the geometry used to model both the alignment offset and lithographic smoothing. Compared to the ideal device simulations shown in Fig. 2c-d, we made the following modifications:

1) A sinusoidal waveguide profile was used instead of a rectangular profile with the modulation amplitude reduced from our ideal design of ±40 nm to ±12 nm. This amplitude reduction was chosen based on our SEM image and empirically measured lithographic smoothing results for Bragg gratings fabricated by ebeam lithography reported in Figure 4.43 of [11].

2) The change in the waveguide's effective index was reduced by 40% for both the amorphous and crystalline states (i.e., less Sb_2Se_3 material is interacting with the waveguide mode). Since we see a reduction in the Bragg bandwidth for both the crystalline and amorphous states, we attribute this to a combination of a vertical offset of Sb_2Se_3 from the waveguide center and a thinner deposited Sb_2Se_3 layer. The refractive index of the Sb_2Se_3 itself remained unchanged from the values in Fig. 1b.

3) A $\pi/2$ offset was used (i.e., a 79 nm offset in the x-direction for a period of 317 nm) to account for misalignment with the Bragg grating. This offset agrees well with the SEM image of the fabricated device.

4) A gaussian transmission profile with 5.8dB of insertion loss was used to account for the ~6dB insertion loss per grating coupler.

Fig. 4d compares the measured full spectra from Fig. 4f with simulated spectra using the above modifications to account for fabrication nonidealities. We see good agreement between the measured and simulated spectra once these nonidealities are accounted for. While the misalignment and differences in waveguide width prevent us from switching between an enabled and disabled Bragg grating, the devices still display an expected increase in $\bar{n}_{eff}$ of the grating to produce a λ_B red shift of approximately 5 nm. The red shift, in turn, leads to extinction ratios of ~20 dB for the wavelengths outside the overlapping stopbands as shown in Fig. 4e-f. Upon crystallization, Fig. 4e-f also exhibit broadening of the stopband bandwidth, which corresponds to an expected increase in Δn_{eff} between segments. Fig. 4e exhibits a response for a device with only N = 200 periods while the devices in Fig. 4f had N = 400 periods. The uniform response versus number of periods can be attributed to accumulation of phase error in the Bragg mirrors.

Fig. 5a-b show SEM images of the fabricated FP devices. As with the Bragg filter devices, both designs exhibit fabrication imperfections, though the evanescent FP design is much more tolerant to small misalignments than the Bragg filter due to the relative size of the Sb_2Se_3 area compared to the alignment accuracy. Fig. 5a shows an embedded PCM device with an incomplete filling of the trench by the phase change material and the passivation layer, which similarly led to devices unresponsive to thermal annealing. In contrast, some misalignment of the PCM over the FP cavity in the evanescent devices did not lead to major changes in expected performance. Fig. 5c shows an effective device which shifts the passband out of the stopband's bandwidth upon crystallization, and Fig. 5d exhibits a device with a 1.583 nm shifting of the passband upon crystallization with extinction ratios of exceeding 25 dB. The device in Fig. 5c used an FP defect that was designed to be 5.425 μm long on a 470 nm wide waveguide. The passband of the device in Fig. 5c exhibits a Q factor of about 1.6×10^4 while the device in Fig. 5d exhibits Q factors of 8.3×10^3 and 4.0×10^3 in the amorphous and crystalline phases respectively. The shift in resonance wavelength of the FP cavity upon phase transition is independent of the average width or number of periods of the Bragg reflectors (minimum number of periods was 100), but is proportional to changes in the FP defect length and modulation strength of Δn_{eff} in the width-modulated passive Bragg mirrors (denoted as Δw in Fig. 5f). The increase in red shift with respect to Δn_{eff} (which is proportional to Δw) between

segments agrees with TMM simulations where FP length and $\bar{n}_{eff}$ are held constant for the given geometries that are shown in Fig. 5. The experimental passband red shift was measured in 23 devices, as plotted in Fig. 5e and fitted as a function of FP cavity length (linearly) and to the width difference between segments in the Bragg mirrors (quadratically). Devices which exhibited larger shifts, such as the device in Fig. 5d, did exist but were not plotted in Fig. 5e since the peak was unable to be measured within the stopband region. The derived contour lines for Δw are shown in Fig. 5f.
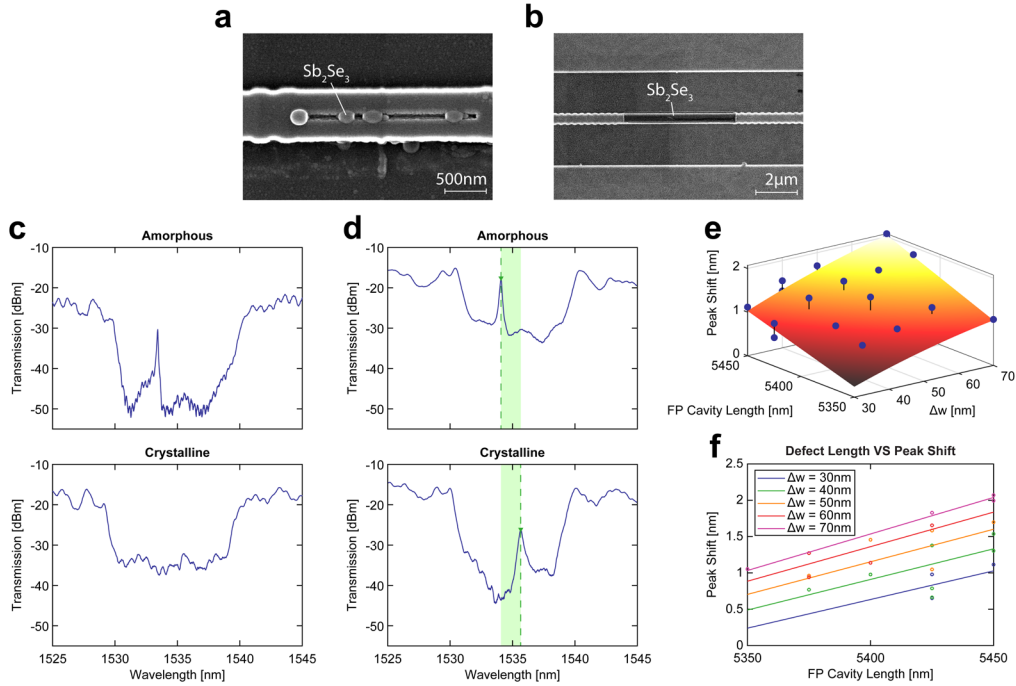

Fig. 5. Results of fabricated Fabry-Perot devices. (a)-(b) SEM Images of fabricated devices. Devices with Sb_2Se_3 (a) embedded and (b) evanescently coupled on the defect segment of a FP device. The poor quality of the filling of the Sb_2Se_3 in the embedded waveguide resulted in minimal effects after crystallization. The phase-shifted device shown in (b) is much less sensitive to alignment compared to the Bragg grating design (Fig. 4a). (c)-(d) Spectra of devices with Sb_2Se_3 deposited on top of the defect. The device in (c) shows an example of expected device behavior. Device in (d) exhibits the characteristic red shift of the passband. Passband peak shift was shown to be related to both FP cavity length and Δw of the Bragg reflectors and is shown in (e)-(f).

5. CONCLUSION

We have proposed and experimentally explored nonvolatile tunable devices using Bragg gratings with various designs and functionalized with Sb_2Se_3. While our experimental results demonstrate the feasibility of the different tunable designs simulated in Section 3, we note that more work is needed to address nonidealities due to the fabrication process—especially misalignment between the waveguide and the phase-change layer. Despite these nonidealities, we have observed Bragg grating devices with stopband shifts of ~5 nm and extinction ratios up to 20 dB upon phase transition, demonstrating the feasibility of using low-loss SbSe to tune the filter response in Bragg gratings. Additionally, we have explored FP cavity devices whose resonances can be shifted as a function of geometrical parameter of the Sb_2Se_3 cell leading to extinction ratios of ~20 dB. Finally, we explored Bragg devices using both embedded and evanescently coupled PCM to enable and disable the Bragg reflection within a waveguide and found that, while the embedded design displays the strongest modulation, an evanescent

approach is more practical when considering fabrication. We envision these devices can be readily integrated into photonic integrated circuits featuring doped-silicon microheaters for electrically controlled reversible switching [21], [25], [33]–[35]. Our results provide new insights into designing zero-static power, reconfigurable Bragg gratings for optical filtering and routing in photonic integrated circuits.

Disclosures. The authors declare no conflicts of interest.

Data availability. Data underlying the results presented in this paper are not publicly available at this time but may be obtained from the authors upon reasonable request.

References

[1]   V. Snigirev *et al.*, "Ultrafast tunable lasers using lithium niobate integrated photonics," *Nature*, vol. 615, no. 7952, pp. 411–417, Mar. 2023, doi: 10.1038/s41586-023-05724-2.

[2]   D. Huang *et al.*, "High-power sub-kHz linewidth lasers fully integrated on silicon," *Optica*, vol. 6, no. 6, p. 745, Jun. 2019, doi: 10.1364/OPTICA.6.000745.

[3]   B. Pan *et al.*, "Compact electro-optic modulator on lithium niobate," *Photonics Res*, vol. 10, no. 3, p. 697, Mar. 2022, doi: 10.1364/PRJ.449172.

[4]   M. Yu *et al.*, "Integrated femtosecond pulse generator on thin-film lithium niobate," *Nature*, vol. 612, no. 7939, pp. 252–258, Dec. 2022, doi: 10.1038/s41586-022-05345-1.

[5]   X. Zhang, K. Kwon, J. Henriksson, J. Luo, and M. C. Wu, "A large-scale microelectromechanical-systems-based silicon photonics LiDAR," *Nature*, vol. 603, no. 7900, pp. 253–258, Mar. 2022, doi: 10.1038/s41586-022-04415-8.

[6]   J. Liu *et al.*, "Monolithic piezoelectric control of soliton microcombs," *Nature*, vol. 583, no. 7816, pp. 385–390, Jul. 2020, doi: 10.1038/s41586-020-2465-8.

[7]   J. Feldmann *et al.*, "Parallel convolutional processing using an integrated photonic tensor core," *Nature*, vol. 589, no. 7840, pp. 52–58, Jan. 2021, doi: 10.1038/s41586-020-03070-1.

[8]   F. Brückerhoff-Plückelmann *et al.*, "Broadband photonic tensor core with integrated ultra-low crosstalk wavelength multiplexers," *Nanophotonics*, vol. 11, no. 17, pp. 4063–4072, Aug. 2022, doi: 10.1515/nanoph-2021-0752.

[9]   X. Xu *et al.*, "11 TOPS photonic convolutional accelerator for optical neural networks," *Nature*, vol. 589, no. 7840, pp. 44–51, Jan. 2021, doi: 10.1038/s41586-020-03063-0.

[10] C. Sun *et al.*, "Single-chip microprocessor that communicates directly using light," *Nature*, vol. 528, no. 7583, pp. 534–538, 2015, doi: 10.1038/nature16454.

[11] L. Chrostowski and M. Hochberg, *Silicon Photonics Design*. Cambridge University Press, 2015. doi: 10.1017/CBO9781316084168.

[12] R. Cheng and L. Chrostowski, "Spectral Design of Silicon Integrated Bragg Gratings: A Tutorial," *Journal of Lightwave Technology*, vol. 39, no. 3, pp. 712–729, Feb. 2021, doi: 10.1109/JLT.2020.3035372.

[13] H. Jayatilleka, K. Murray, M. Caverley, N. A. F. Jaeger, L. Chrostowski, and S. Shekhar, "Crosstalk in SOI Microring Resonator-Based Filters," *Journal of Lightwave Technology*, vol. 34, no. 12, pp. 2886–2896, Jun. 2016, doi: 10.1109/JLT.2015.2480101.

[14] A. Prencipe, M. A. Baghban, and K. Gallo, "Tunable Ultranarrowband Grating Filters in Thin-Film Lithium Niobate," *ACS Photonics*, vol. 8, no. 10, pp. 2923–2930, Oct. 2021, doi: 10.1021/acsphotonics.1c00383.

[15] W. Zhang and J. Yao, "A fully reconfigurable waveguide Bragg grating for programmable photonic signal processing," *Nat Commun*, vol. 9, no. 1, p. 1396, Apr. 2018, doi: 10.1038/s41467-018-03738-3.

[16] J. Faneca *et al.*, "On-chip sub-wavelength Bragg grating design based on novel low loss phase-change materials," *Opt Express*, vol. 28, no. 11, p. 16394, May 2020, doi: 10.1364/OE.389598.

[17] W. Li, C. Qiu, and A. Wu, "Nonvolatile Reconfigurable Phase-Shifted Bragg Grating Filter With Tunable Wavelength and Extinction Ratio," *IEEE Photonics J*, vol. 15, no. 3, pp. 1–7, Jun. 2023, doi: 10.1109/JPHOT.2023.3267276.

[18] T. Zhou *et al.*, "Reconfigurable hybrid silicon waveguide Bragg filter using ultralow-loss phase-change material," *Appl Opt*, vol. 61, no. 7, p. 1660, Mar. 2022, doi: 10.1364/AO.451078.

[19] M. Wuttig and N. Yamada, "Phase-change materials for rewriteable data storage," *Nat Mater*, vol. 6, no. 11, pp. 824–832, Nov. 2007, doi: 10.1038/nmat2009.

[20] M. Wei *et al.*, "Electrically programmable phase-change photonic memory for optical neural networks with nanoseconds in situ training capability," *Advanced Photonics*, vol. 5, no. 04, Jul. 2023, doi: 10.1117/1.AP.5.4.046004.

[21] C. Ríos *et al.*, "Ultra-compact nonvolatile phase shifter based on electrically reprogrammable transparent phase change materials," *PhotoniX*, vol. 3, no. 1, p. 26, Oct. 2022, doi: 10.1186/s43074-022-00070-4.

[22] M. Delaney, I. Zeimpekis, D. Lawson, D. W. Hewak, and O. L. Muskens, "A New Family of Ultralow Loss Reversible Phase-Change Materials for Photonic Integrated Circuits: Sb2S3 and Sb2Se3," *Adv Funct Mater*, vol. 30, no. 36, pp. 1–10, Sep. 2020, doi: 10.1002/adfm.202002447.

[23] M. Delaney *et al.*, "Nonvolatile programmable silicon photonics using an ultralow-loss Sb2Se3 phase change material," *Sci Adv*, vol. 7, no. 25, p. eabg3500, Jun. 2021, doi: 10.1126/sciadv.abg3500.

[24] Z. Fang *et al.*, "Ultra-low-energy programmable non-volatile silicon photonics based on phase-change materials with graphene heaters," *Nat Nanotechnol*, vol. 17, no. 8, pp. 842–848, Aug. 2022, doi: 10.1038/s41565-022-01153-w.

[25] D. Wu *et al.*, "Resonant multilevel optical switching with phase change material GST," *Nanophotonics*, vol. 11, no. 15, pp. 3437–3446, Aug. 2022, doi: 10.1515/nanoph-2022-0276.

[26] H. Hu *et al.*, "Contra-directional switching enabled by Si-GST grating," *Opt Express*, vol. 28, no. 2, p. 1574, Jan. 2020, doi: 10.1364/OE.381502.

[27] A. Sebastian, M. Le Gallo, and D. Krebs, "Crystal growth within a phase change memory cell," *Nat Commun*, vol. 5, no. 1, p. 4314, Dec. 2014, doi: 10.1038/ncomms5314.

[28] J. Feldmann *et al.*, "Calculating with light using a chip-scale all-optical abacus," *Nat Commun*, vol. 8, no. 1, p. 1256, Dec. 2017, doi: 10.1038/s41467-017-01506-3.

[29] C.-C. Popescu *et al.*, "An Open-Source Multi-functional Testing Platform for Optical Phase Change Materials," Jul. 2023, [Online]. Available: http://arxiv.org/abs/2307.06216

[30] J. Meng *et al.*, "Electrical programmable multilevel nonvolatile photonic random-access memory," *Light Sci Appl*, vol. 12, no. 1, p. 189, Aug. 2023, doi: 10.1038/s41377-023-01213-3.

[31] R. Chen *et al.*, "Non-volatile electrically programmable integrated photonics with a 5-bit operation," *Nat Commun*, vol. 14, no. 1, p. 3465, Jun. 2023, doi: 10.1038/s41467-023-39180-3.

[32] Y. Zhang *et al.*, "Broadband transparent optical phase change materials for high-performance nonvolatile photonics," *Nat Commun*, vol. 10, no. 1, p. 4279, Dec. 2019, doi: 10.1038/s41467-019-12196-4.

[33] R. Chen, Z. Fang, J. E. Fröch, P. Xu, J. Zheng, and A. Majumdar, "Broadband Nonvolatile Electrically Controlled Programmable Units in Silicon Photonics," *ACS Photonics*, vol. 9, no. 6, pp. 2142–2150, Jun. 2022, doi: 10.1021/acsphotonics.2c00452.

[34] J. Zheng *et al.*, "Nonvolatile Electrically Reconfigurable Integrated Photonic Switch Enabled by a Silicon PIN Diode Heater," *Advanced Materials*, vol. 32, no. 31, p. 2001218, Aug. 2020, doi: 10.1002/adma.202001218.

[35] H. Zhang *et al.*, "Nonvolatile waveguide transmission tuning with electrically-driven ultra-small GST phase-change material," *Sci Bull (Beijing)*, vol. 64, no. 11, pp. 782–789, Jun. 2019, doi: 10.1016/j.scib.2019.04.035.